Frequency-domain system identification of nonlinear structures using experimental continuation data

Frequency-domain system identification of nonlinear structures using experimental continuation data

Dario Anastasio[1*], Ghislain Raze[2], Gaëtan Kerschen[2]

[1] *Department of Mechanical and Aerospace Engineering, Politecnico di Torino, Torino, Italy*
[2] *Aerospace and Mechanical Engineering Department, University of Liege, Liège, Belgium*

https://doi.org/10.1177/10775463251405337

Abstract

This work introduces a nonlinear system identification method that uses frequency response data to estimate a compact and interpretable nonlinear state-space model of structural systems. A key novelty is the ability to directly exploit data from experimental continuation, including unstable branches, by minimizing the discrepancy between measured and predicted outputs across multiple harmonics. This enables accurate characterization of nonlinear dynamics from a limited dataset, while keeping computational costs low and ensuring robustness to noise and initialization. The method, called NFR-ID, is validated through two experimental cases: an electronic Duffing oscillator and a thin-walled plate, the latter exhibiting rich nonlinear behavior due to large-amplitude vibrations. Results demonstrate the accuracy and broad applicability of NFR-ID as an efficient and general framework for analyzing nonlinear structural dynamics.

Keywords

nonlinear system identification; frequency response; experimental continuation; control-based continuation; nonlinear vibrations; thin-walled structures; state-space.

Declaration of conflicting interests

The author(s) declared no potential conflicts of interest with respect to the research, authorship, and/or publication of this article.

Data availability

The datasets generated during and/or analyzed during the current study are available from the corresponding author on reasonable request.

Funding

The author(s) disclosed receipt of the following financial support for the research, authorship, and/or publication of this article: Ghislain Raze is a Postdoctoral Researcher of the Fonds de la Recherche Scientifique — FNRS, which is gratefully acknowledged.

---

[*] *Corresponding author: dario.anastasio@polito.it*

1. Introduction

In recent years, increasing attention has been devoted to understanding and predicting nonlinear dynamic behavior in structural systems. Nonlinearities are often inherent characteristics of real-world structures – arising from sources such as large deformations, boundary conditions, material behavior, or contact interfaces – and can strongly affect structural performance under dynamic loading. In some cases, nonlinear features are intentionally designed to trigger effects unfeasible with a linear behavior (Gatti et al., 2019; Nayfeh and Mook, 1995). In this regard, developing nonlinear models directly from experimental data has become an increasingly popular approach. This process, known as "nonlinear system identification", has led to the development of several methods that address the growing complexity of engineering structures (Kerschen et al., 2006; Noël and Kerschen, 2017). However, despite advancements, nonlinear system identification remains a complex and challenging exercise, particularly when aiming for models suitable for performance assessment and predictive tasks.

Many existing techniques rely on time-domain data to construct a model, as it generally provides rich dynamic information for capturing nonlinear behaviors. This has enabled the use of tools such as Hilbert transform (Feldman et al., 2009; Kerschen et al., 2008), Volterra series (Demarie et al., 2011; Worden and Tomlinson, 2001) and subspace approaches (Marchesiello and Garibaldi, 2008). Other methods exploit time-domain broadband data to estimate a frequency-domain model, such as (Paduart et al., 2010) and (Noël and Kerschen, 2013). The broader field of data-driven methods also includes techniques like Dynamic Mode Decomposition (DMD) and machine learning approaches (Kutz, 2016). DMD extracts low-rank spatiotemporal features and provides linear surrogates of nonlinear dynamics, while machine learning offers highly flexible black-box models. Although powerful, these methods often lack physical interpretability and may require large datasets, which can limit their practicality for experimental testing and standard industrial practices in structural dynamics. In contrast, frequency-domain measurements are widely used in validation and qualification protocols across many engineering sectors, offering a condensed representation of steady-state dynamic behavior. Exploiting such data for nonlinear identification is therefore appealing, as it could streamline modeling workflows and reduce the need for dedicated campaigns.

Despite these advantages, the direct use of nonlinear frequency responses (NFRs) for identification remains constrained by several limitations. Some methods (Arslan et al., 2011; Carrella and Ewins, 2011; Jalali and Bonab, 2013; Maio, 2025) extract amplitude-dependent equivalent modal parameters from measured NFRs. While useful for characterization, such approaches do not deliver a complete nonlinear model of the system and are restricted in the types and strengths of nonlinearities they can address. A related strategy updates the linear FRFs of a nonlinear structure from NFRs measured at different excitation levels (Canbaloğlu and Özgüven, 2016). A more comprehensive approach has been proposed in (Taghipour et al., 2022), based on the (multi) harmonic balance method (HBM). Yet, it requires prior knowledge of the underlying linear system (ULS) and direct updating of the governing equations, which limits its general applicability.

One challenge in NFR measurements is that nonlinear systems tend to exhibit super- and/or sub-harmonics of the excitation frequency, unstable solutions branches and internal resonances. This raises questions about how to define and experimentally measure the frequency response. From a modeling perspective, HBM is commonly used to compute these responses from a known model in combination with a numerical continuation technique (Detroux et al., 2015). On the experimental side, the direct measurement of full NFRs, including unstable solutions, is far more difficult. Methods for "experimental continuation" replicate numerical continuation using feedback control loops and iterative testing, including control-based continuation (CBC) (Barton et al., 2012; Sieber and Krauskopf, 2008), simplified CBC (Barton and Sieber, 2013), phase-locked loops (Peter and Leine, 2017), response-controlled testing (RCT) (Karaağaçlı and Özgüven, 2020, 2021), and arclength CBC (ACBC) (Raze et al., 2025). All these approaches lead to a set of input-output data that builds up a portion of the bifurcation diagram of the system. In this context, the NFR obtained by experimental continuation will be here referred to as "non-parametric" and generally includes both stable and unstable paths. For specific implementations of such methods, we refer to the recent review paper (Raze et al., 2025). Notably, Karaağaçlı and Özgüven (2021) also implement the extraction of amplitude-dependent modal parameters with RCT. The use of experimental continuation data to identify a nonlinear model of the system was attempted in two recent works (Beregi et al., 2021; Mélot et al., 2024), although they rely on case-specific formulations of the cost function.

These considerations highlight the need for a general framework that can use experimentally measured NFRs to construct fully nonlinear models suitable for predictive purposes in the context of structural dynamics. This work addresses this need by presenting a nonlinear frequency response-based identification framework, termed NFR-ID. The method estimates a nonlinear state-space model of the system solving a nonlinear minimization problem and can handle multi-harmonic measurement, when available, as well as unstable solution paths. Nonlinearities are represented as extensions to an underlying linear system – a modeling paradigm shown to be effective in multiple prior studies (Anastasio and Marchesiello, 2023; Marchesiello and Garibaldi, 2008; Noël and Kerschen, 2013; Zhu et al., 2023) – and captured through a set of candidate nonlinear basis functions. Owing to its general formulation, NFR-ID can be applied to a broad range of nonlinear systems, including single- and multi-degree-of-freedom configurations, continuous elements, and complex structural assemblies. It can be applied to a variety of structural applications, where frequency-domain tests are routinely performed using commercial testing software and standardized procedures.

The paper is structured as follows. Section 2 introduces and discusses the proposed methodology. Section 3 presents the application of the method to an electronic Duffing oscillator, while Section 4 extends the analysis to a clamped-free thin plate. For each case, multiple validation sets are used to assess the prediction capability of the estimated model. Finally, conclusions are provided in Section 5.

2. NFR-ID method

This section describes the proposed identification method, referred to as NFR-ID. The methodology is structured around three main parts, as outlined in the high-level flowchart in Fig. 1. Detailed steps are discussed in the following sections.

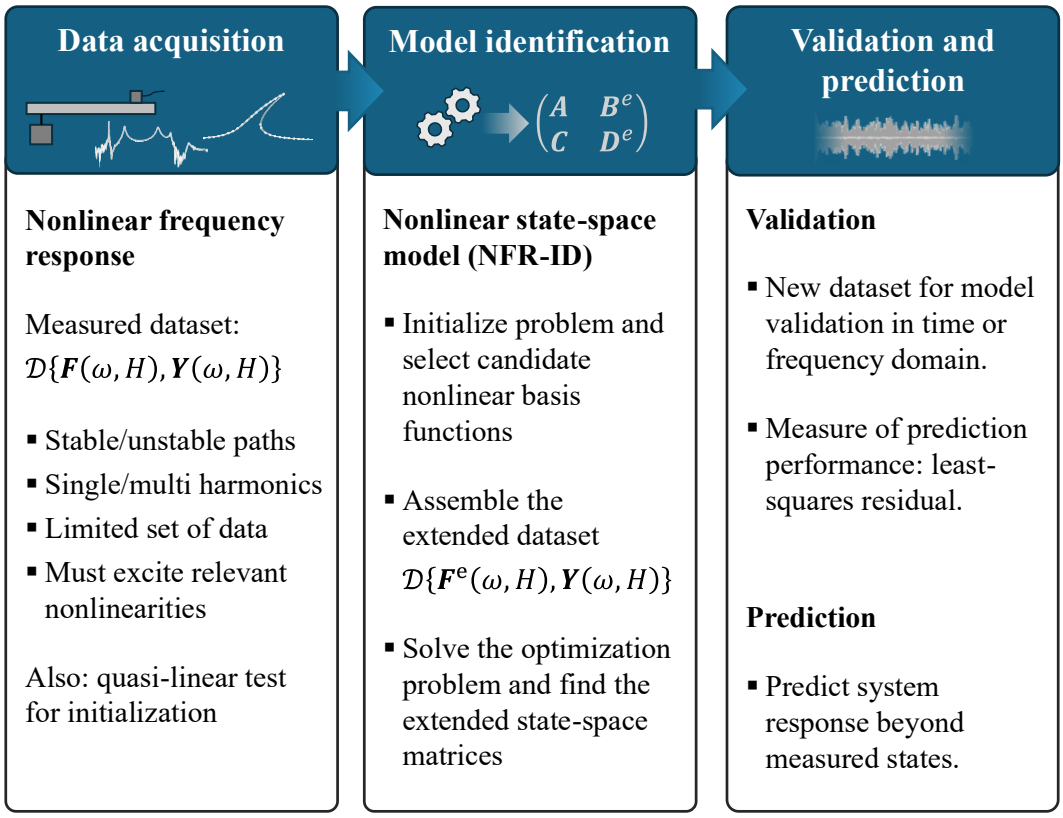

Fig. 1. Overview of the NFR-ID framework.

2.1. Data acquisition

The data used for the identification method is assumed to be in the form of a non-parametric nonlinear frequency response (NFR) from a generic multi-degree-of-freedom (DOF) system. The problem can be also adapted to continuous structures, as in Section 4. The measured non-parametric NFR is defined as the following input-output dataset with p inputs and q outputs:

$$\mathcal{D}\{\boldsymbol{F}(\omega,H),\ \boldsymbol{Y}(\omega,H)\}.$$

Here, it is assumed that the input and output vectors, $\boldsymbol{F}$ and $\boldsymbol{Y}$, originate from a Fourier series representation up to order H of this kind:

$$\begin{aligned} \boldsymbol{y}(t) &= \boldsymbol{Y}^{(0)} + \sum_{h=1}^{H} \left(\boldsymbol{Y}_{\mathrm{c}}^{(h)} \cos(h\omega t) + \boldsymbol{Y}_{\mathrm{s}}^{(h)} \sin(h\omega t) \right) \in \mathbb{R}^{q}, \\ \boldsymbol{f}(t) &= \boldsymbol{F}^{(0)} + \sum_{h=1}^{H} \left(\boldsymbol{F}_{\mathrm{c}}^{(h)} \cos(h\omega t) + \boldsymbol{F}_{\mathrm{s}}^{(h)} \sin(h\omega t) \right) \in \mathbb{R}^{p}. \end{aligned} \tag{1}$$

The vectors $\boldsymbol{F}$ and $\boldsymbol{Y}$ stack cosine and sine coefficients as:

$$\begin{aligned}\boldsymbol{Y} &= \left[\boldsymbol{Y}^{(0)^{\mathrm{T}}}, \quad \boldsymbol{Y}_{\mathrm{c}}^{(1)^{\mathrm{T}}}, \quad \boldsymbol{Y}_{\mathrm{s}}^{(1)^{\mathrm{T}}}, \quad \dots, \quad \boldsymbol{Y}_{\mathrm{c}}^{(H)^{\mathrm{T}}}, \quad \boldsymbol{Y}_{\mathrm{s}}^{(H)^{\mathrm{T}}}\right]^{\mathrm{T}}, \\ \boldsymbol{F} &= \left[\boldsymbol{F}^{(0)^{\mathrm{T}}}, \quad \boldsymbol{F}_{\mathrm{c}}^{(1)^{\mathrm{T}}}, \quad \boldsymbol{F}_{\mathrm{s}}^{(1)^{\mathrm{T}}}, \quad \dots, \quad \boldsymbol{F}_{\mathrm{c}}^{(H)^{\mathrm{T}}}, \quad \boldsymbol{F}_{\mathrm{s}}^{(H)^{\mathrm{T}}}\right]^{\mathrm{T}},\end{aligned} \tag{2}$$

so that eq. (2) can be written in the following compact form:

$$\begin{aligned}\boldsymbol{y}(t) &= \left(\boldsymbol{Q}(t) \otimes \boldsymbol{I}_q\right)\boldsymbol{Y}, \\ \boldsymbol{f}(t) &= \left(\boldsymbol{Q}(t) \otimes \boldsymbol{I}_p\right)\boldsymbol{F},\end{aligned} \tag{3}$$

where $\boldsymbol{Q}(t) = [1 \quad \cos(\omega t) \quad \sin(\omega t) \quad \dots \quad \cos(H\omega t) \quad \sin(H\omega t)]$ is a linear operator, $\otimes$ denotes the Kronecker product and $\boldsymbol{I}_k$ is the identity matrix of size k.

The dataset $\mathcal{D}$ can be obtained experimentally through various methods and generally it includes stable and unstable response paths. Capturing unstable paths from experimental tests is feasible using an experimental continuation technique. Two cases will be distinguished in the following (Fig. 2):

i. Full NFR measurement (stable and unstable paths): this can be achieved by employing an experimental continuation technique. For this class of methods to work properly, the controller must be of non-invasive kind, as outlined in (Raze et al., 2025).

ii. Stable-only NFR measurement: this occurs in tests such as stepped-sine vibration experiments, which are performed to determine the steady-state nonlinear response of the structure at various frequencies without continuation (Taghipour et al., 2022). Unstable paths (if any) are not detected in this case, and the response is likely to exhibit jumps. This is also the case of several commercial software tools and industry standards, which are often based on frequency-domain tests. In such cases, only the fundamental harmonic is typically stored, which can be considered a special case of multi-harmonic testing.

The frequency range of the data is likely to encompass primary and/or secondary resonances of the system. The measured data used in this study originates from experimental continuation tests; therefore, case (i) is considered. The proposed method can also be adapted to case (ii) by excluding the unmeasured regions from the analysis, at the cost of reduced available information to train the model.

It is worth noticing that the highest measurable harmonic contribution is constrained by the Nyquist theorem. If f_{max} denotes the maximum frequency of interest and f_s the sampling frequency, it follows that $H < f_s/(2f_{max})$. However, the actual number of harmonics worth including in the optimization process depends on the specific case and can be determined by examining the dominant harmonic components in the experimental data through Fourier signal decomposition.

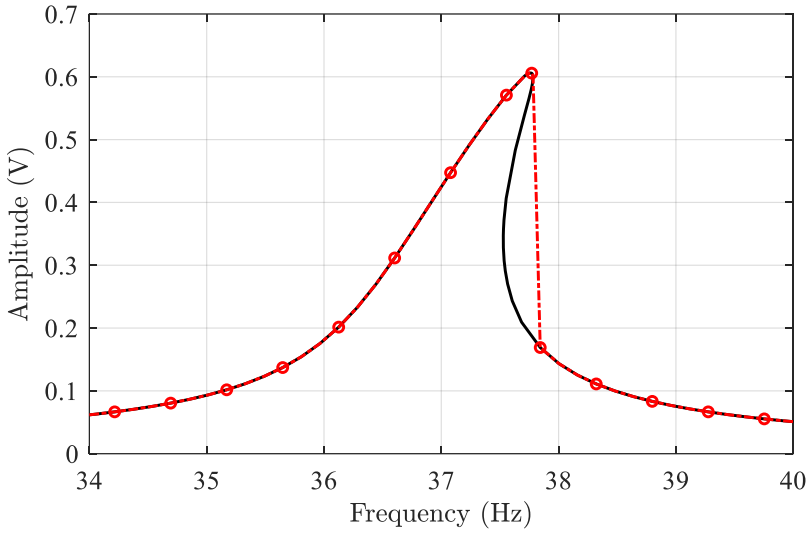

Fig. 2. Example of full NFR (black line) and stable-only NFR (circled dashed-dotted red line) with jump.

2.1.1. ACBC method

This section provides a brief outlook of the ACBC method for experimental continuation. The reader is referred to (Raze et al., 2025) for detailed implementation.

Following the principles of control-based continuation, ACBC excites the structure using the output of a proportional-derivative (PD) controller. The force acting on the structure is therefore written in terms of differential and proportional gains, $k_{\mathrm{d,y}}$ and $k_{\mathrm{p,y}}$, respectively. This controller can stabilize an equilibrium in which the measured output $y(t)$ closely follows the target signal $y_*(t)$. Since the goal of the test is to measure an NFR while ensuring non-invasiveness of the controller, this target signal is adjusted to make an equilibrium of the closed-loop system identical to that of the open-loop system. This condition is met when the output of the controller is equal to the desired excitation profile while the structure follows one of its periodic orbits. Typically, this desired excitation takes the form of a harmonic signal with prescribed amplitude.

To maintain non-invasiveness, ACBC modifies the target signal, separating it into fundamental and non-fundamental harmonics. The non-fundamental harmonics of the target signal are synchronized with the response using an online Fourier decomposition with adaptive filters (Abeloos et al., 2021), ensuring harmonic excitation. The fundamental harmonic is then adjusted to achieve the desired excitation amplitude.

ACBC employs a derivative-free arclength continuation algorithm to track the NFR. It iteratively refines excitation parameters by defining an elliptical path around the current point and adjusting parameters until the desired forcing amplitude is reached. This process is repeated point by point to construct the NFR.

2.2. Model identification

2.2.1. Problem statement

The problem statement of the proposed method takes the form of a nonlinear state-space model of size n in the *extended* formulation (Marchesiello and Garibaldi, 2008). Considering a continuous time-domain representation, this yields:

$$\begin{cases} \dot{\boldsymbol{x}}(t) = \boldsymbol{A}\boldsymbol{x}(t) + \boldsymbol{B}^{\mathrm{e}}\boldsymbol{f}^{\mathrm{e}}(\boldsymbol{y}, \dot{\boldsymbol{y}}, t) \\ \boldsymbol{y}(t) = \boldsymbol{C}\boldsymbol{x}(t) + \boldsymbol{D}^{\mathrm{e}}\boldsymbol{f}^{\mathrm{e}}(\boldsymbol{y}, \dot{\boldsymbol{y}}, t) \end{cases}, \tag{4}$$

where $\boldsymbol{y}(t) \in \mathbb{R}^q$ is the output vector, $\boldsymbol{x}(t) \in \mathbb{R}^n$ is the state vector and $\boldsymbol{f}^{\mathrm{e}}$ is the so-called extended-input vector. This vector stacks the measured input vector $\boldsymbol{f}(t) \in \mathbb{R}^p$ with a vector $\boldsymbol{g}_{\mathrm{nl}}(\boldsymbol{y}, \dot{\boldsymbol{y}}, t)$ containing a collection of J nonlinear basis functions used to describe the functional behavior of the nonlinearities of the system:

$$\boldsymbol{g}_{\mathrm{nl}}(\boldsymbol{y}, \dot{\boldsymbol{y}}, t) = \left[-g_1(\boldsymbol{y}, \dot{\boldsymbol{y}}, t), \quad \dots, \quad -g_J(\boldsymbol{y}, \dot{\boldsymbol{y}}, t)\right]^{\mathrm{T}}. \tag{5}$$

These functions are assumed to be known and form a library of feasible functions. Alternatively, the use of splines can be exploited as in (Noël et al., 2014). The extended-input vector $\boldsymbol{f}^{\mathrm{e}}$ is therefore defined as:

$$\boldsymbol{f}^{\mathrm{e}}(\boldsymbol{y}, \dot{\boldsymbol{y}}, t) = [\boldsymbol{f}(t)^{\mathrm{T}}, \quad \boldsymbol{g}_{\mathrm{nl}}(\boldsymbol{y}, \dot{\boldsymbol{y}}, t)^{\mathrm{T}}]^{\mathrm{T}}. \tag{6}$$

The matrices $\boldsymbol{A}, \boldsymbol{B}^{\mathrm{e}}, \boldsymbol{C}, \boldsymbol{D}^{\mathrm{e}}$ of eq. (4) are the state, extended input, output and extended direct feedthrough matrices, respectively. It is worth noticing that the matrix $\boldsymbol{A}$ is the state-matrix of the underlying linear system, thus the underlying-linear dynamics of the structure can be easily estimated by classical eigenvalue decomposition of $\boldsymbol{A}$. All the steps described in this section refer to the continuous formulation for simplicity. Transformations to the discrete formulation can be performed as in (Marchesiello and Garibaldi, 2008).

The state-space model of eq. (4) can be written in the frequency domain by applying the harmonic balance method, with the transformations of eq. (1) applied to output, state and external forces vectors. Detailed steps are reported in (Anastasio and Marchesiello, 2023), and the formulation reads:

$$\begin{cases} (\boldsymbol{\nabla} \otimes \boldsymbol{I}_n)\boldsymbol{X} = (\boldsymbol{I}_{\widetilde{H}} \otimes \boldsymbol{A})\boldsymbol{X} + (\boldsymbol{I}_{\widetilde{H}} \otimes \boldsymbol{B}^{\mathrm{e}})\boldsymbol{F}^{\mathrm{e}} \\ \boldsymbol{I}_{q\widetilde{H}}\boldsymbol{Y} = (\boldsymbol{I}_{\widetilde{H}} \otimes \boldsymbol{C})\boldsymbol{X} + (\boldsymbol{I}_{\widetilde{H}} \otimes \boldsymbol{D}^{\mathrm{e}})\boldsymbol{F}^{\mathrm{e}} \end{cases}. \tag{7}$$

Here, $\widetilde{H} = 2H + 1$. The vectors $\boldsymbol{X}$, $\boldsymbol{Y}$ and $\boldsymbol{F}^{\mathrm{e}}$ contain the Fourier coefficients of the corresponding time vectors $\boldsymbol{x}$, $\boldsymbol{y}$ and $\boldsymbol{f}^{\mathrm{e}}$, as in eq. (1).

The operator $\boldsymbol{\nabla}$ in eq. (7) is defined as:

$$\boldsymbol{\nabla} = \mathrm{diag}(0, \quad \boldsymbol{\nabla}_1, \quad \dots, \quad \boldsymbol{\nabla}_H), \quad \boldsymbol{\nabla}_h = h\omega \begin{bmatrix} 0 & 1 \\ -1 & 0 \end{bmatrix}. \tag{8}$$

The input-output relation can be obtained by rearranging eq. (7) as

$$\boldsymbol{I}_{q\tilde{H}}\boldsymbol{Y} = [(\boldsymbol{I}_{\tilde{H}} \otimes \boldsymbol{D}^{\mathrm{e}}) + (\boldsymbol{I}_{\tilde{H}} \otimes \boldsymbol{C})(\boldsymbol{\nabla} \otimes \boldsymbol{I}_n - \boldsymbol{I}_{\tilde{H}} \otimes \boldsymbol{A})^{-1}(\boldsymbol{I}_{\tilde{H}} \otimes \boldsymbol{B}^{\mathrm{e}})]\, \boldsymbol{F}^{\mathrm{e}} = \boldsymbol{\Lambda}^{\mathrm{e}}\boldsymbol{F}^{\mathrm{e}}. \tag{9}$$

The matrix $\boldsymbol{\Lambda}^{\mathrm{e}}$ relates the inputs to the outputs for each frequency ω, and is a function of the state-space matrices. As for the vector $\boldsymbol{F}^{\mathrm{e}}$, it contains the Fourier coefficients of both the forcing term and the nonlinear basis functions. The latter depend on displacements and/or velocities, and therefore their Fourier coefficients are a function of $\boldsymbol{Y}$. The stability of the periodic solutions to the state-space model of eq. (7) can be inspected as reported in (Anastasio and Marchesiello, 2023).

2.2.2. Identification procedure

Starting from the measured input-output dataset $\mathcal{D}\{\boldsymbol{F}(\omega, H), \boldsymbol{Y}(\omega, H)\}$ in the frequency domain, the initial step involves constructing the vector of Fourier coefficients of the nonlinear basis functions, $\boldsymbol{G}_{\mathrm{nl}}$, which is defined analogously to eq. (1). This process can be efficiently performed using the alternating frequency/time-domain (AFT) technique (Cameron and Griffin, 1989). In the proposed approach, the AFT algorithm utilizes the inverse Fourier transform to compute the nonlinear basis functions $g_j(\boldsymbol{y}, \dot{\boldsymbol{y}}, t),\ j = 1, \dots, J$, in the time domain for each ω. The vector $\boldsymbol{G}_{\mathrm{nl}}$ is then obtained by switching back to the frequency domain:

$$\boldsymbol{Y}(\omega, H) \xrightarrow{\mathrm{FFT}^{-1}} \big(\boldsymbol{y}(t), \dot{\boldsymbol{y}}(t)\big) \rightarrow \boldsymbol{g}_{\mathrm{nl}}(t) = \big[-g_1, \quad \dots, \quad -g_J\big]^{\mathrm{T}} \xrightarrow{\mathrm{FFT}} \boldsymbol{G}_{\mathrm{nl}}(\omega, H). \tag{10}$$

The extended input vector is thus given by:

$$\boldsymbol{F}^{\mathrm{e}}(\omega, H) = [\boldsymbol{F}^{\mathrm{T}}, \quad \boldsymbol{G}_{\mathrm{nl}}^{\mathrm{T}}]^{\mathrm{T}}. \tag{11}$$

If $\boldsymbol{Y}_{\mathrm{m}}$ is the output of an (unknown) model in the form of eq. (9), with input equal to $\boldsymbol{F}^{\mathrm{e}}$, an optimization problem can be formulated to minimize the error $\boldsymbol{\epsilon} = (\boldsymbol{Y}_{\mathrm{m}} - \boldsymbol{Y})$. Note that $\boldsymbol{\epsilon}$ is a real quantity, given the definitions of eq. (2).

The parameters to be optimized are the entries of the matrices $\boldsymbol{A}, \boldsymbol{B}^{\mathrm{e}}, \boldsymbol{C}, \boldsymbol{D}^{\mathrm{e}}$, which are structured into a parameter vector $\boldsymbol{\theta} = [\mathrm{vec}(\boldsymbol{A});\ \mathrm{vec}(\boldsymbol{B}^{\mathrm{e}});\ \mathrm{vec}(\boldsymbol{C});\ \mathrm{vec}(\boldsymbol{D}^{\mathrm{e}})]$, with $\mathrm{vec}(\cdot)$ vectorization operator. The minimization problem thus reads:

$$\widehat{\boldsymbol{\theta}} = \underset{\boldsymbol{\theta}}{\mathrm{argmin}}\, \boldsymbol{\epsilon} = \underset{\boldsymbol{\theta}}{\mathrm{argmin}} \left(\left|\left|\boldsymbol{Y}_{\mathrm{m}}(\boldsymbol{\theta}) - \boldsymbol{Y}\right|\right|^2\right) = \underset{\boldsymbol{\theta}}{\mathrm{argmin}} \left(\left|\left|\boldsymbol{\Lambda}^{\mathrm{e}}(\boldsymbol{\theta})\boldsymbol{F}^{\mathrm{e}} - \boldsymbol{Y}\right|\right|^2\right). \tag{12}$$

This problem can be approached with different optimization strategies, such as gradient-based, evolutionary, or probabilistic methods. In this work, it is solved using the Levenberg-Marquardt algorithm (Levenberg, 1944; Marquardt, 1963), chosen for its efficiency and robustness in handling nonlinear least-squares problems of moderate size. The algorithm requires the computation of the Jacobian of the model error $\boldsymbol{\epsilon}$ with respect to the model parameters. Luckily, a closed form of the Jacobian matrix $\boldsymbol{J}$ can be obtained in this case, considering that:

$$\boldsymbol{J}(\omega,\boldsymbol{\theta}) = \frac{\partial \boldsymbol{\epsilon}(\omega,\boldsymbol{\theta})}{\partial \boldsymbol{\theta}} = \frac{\partial \boldsymbol{Y}_{\mathrm{m}}(\omega,\boldsymbol{\theta})}{\partial \boldsymbol{\theta}}. \tag{13}$$

The parameter vector $\boldsymbol{\theta}$ stacks the entries of the state-space matrices, which are linked to the model output $\boldsymbol{Y}_{\mathrm{m}}$ by eq. (7). The reader is referred to (Noël and Kerschen, 2013; Paduart et al., 2010) for explicit expressions of the Jacobian matrix within the considered nonlinear state-space formulation.

2.2.3. Problem initialization

The nonlinear problem of eq. (12) can be initialized in two ways:

i. Obtain an initial estimate of the linearized system matrices $\{\boldsymbol{A},\boldsymbol{B},\boldsymbol{C},\boldsymbol{D}\}_{\mathrm{L}}$ directly from the measured dataset $\mathcal{D}$, by applying a linear state-space identification technique in the frequency domain. However, this might be impractical, as $\boldsymbol{Y}$ is likely to exhibit unstable paths and non-unique solutions.

ii. Use an initial estimate of the underlying linear FRF from a (quasi) linear test. Thus, matrices $\{\boldsymbol{A},\boldsymbol{B},\boldsymbol{C},\boldsymbol{D}\}_{\mathrm{ULS}}$ can be estimated using a linear state-space identification technique (Overschee and Moor, 1996).

It is important to note that a preliminary linear or quasi-linear broadband test is typically conducted before any experimental continuation test. This step helps establish the baseline FRF and determine the natural frequencies of the system. Therefore, in this context, the second approach appears to be the most suitable choice. The terminology “quasi-linear” indicates that the system might also exhibit a weak nonlinear behavior at this stage, since all the system matrices will be optimized in the second step. Writing $\boldsymbol{B}^{\mathrm{e}}$ as $\boldsymbol{B}^{\mathrm{e}} = \left[\boldsymbol{B},\ \boldsymbol{B}^{\mathrm{nl}}\right]$ and $\boldsymbol{D}^{\mathrm{e}}$ as $\boldsymbol{D}^{\mathrm{e}} = \left[\boldsymbol{D},\ \boldsymbol{D}^{\mathrm{nl}}\right]$, the entries of matrices $\boldsymbol{B}^{\mathrm{nl}}$ and $\boldsymbol{D}^{\mathrm{nl}}$ related to the nonlinear feedbacks are initialized to zero, and they are later optimized.

2.3. Method overview and assumptions

The key features and assumptions of the NFR-ID method are summarized below.

- Model structure: the system is represented as a nonlinear state-space model, with nonlinearities expressed through a set of basis functions.
- A priori knowledge: the user defines a library of candidate nonlinear basis functions, which requires some prior insights into the system.
- Data quality: the approach is designed for non-parametric nonlinear frequency-response data, possibly containing multi-harmonic content.
- Parameter identification: nonlinear state-space matrices are estimated via least-squares optimization. A good initial estimate of the underlying linear dynamics is used to mitigate the risk of local minima and improve convergence.
- Applicability: the general formulation of the method enables application to a broad range of systems, including single- and multi-degree-of-freedom configurations, as well as continuous structures.

3. Experimental application: electronic Duffing oscillator

The setup discussed in this section consists of an electronic Duffing oscillator - a circuit that emulates the dynamics of a Duffing oscillator. This system is selected as an initial example for its near-perfect actuation and repeatability, while still preserving key experimental characteristics. Despite its simplicity, the Duffing equation plays a significant role in nonlinear structural dynamics (Gatti et al., 2019; Nayfeh and Mook, 1995).

The parameters of the electronic Duffing oscillator can be adjusted using three knobs, which control the damping ratio ζ, the natural frequency ω_n and the cubic stiffness coefficient k_3. Further details about this circuit can be found (Raze, 2024). This circuit was connected to a real-time control unit (MicroLabBox from dSPACE) which was programmed to implement either an experimental continuation approach or to generate a broadband excitation signal.

3.1. Assessment of the initial model

The initial linear state-space model was derived from a low-level broadband test in open-loop condition, lasting for 120 seconds and sampled at 5000 Hz. Subspace identification was used to estimate the state space matrices $\{\boldsymbol{A}, \boldsymbol{B}, \boldsymbol{C}, \boldsymbol{D}\}_{\text{ULS}}$ with a model order equal to 2, based on the singular value distribution shown in Fig. 3a (Overschee and Moor, 1996). The identified underlying linear FRF is displayed in Fig. 3b. The estimated natural frequency and damping ratio are 36.85 Hz and 0.7%, respectively.

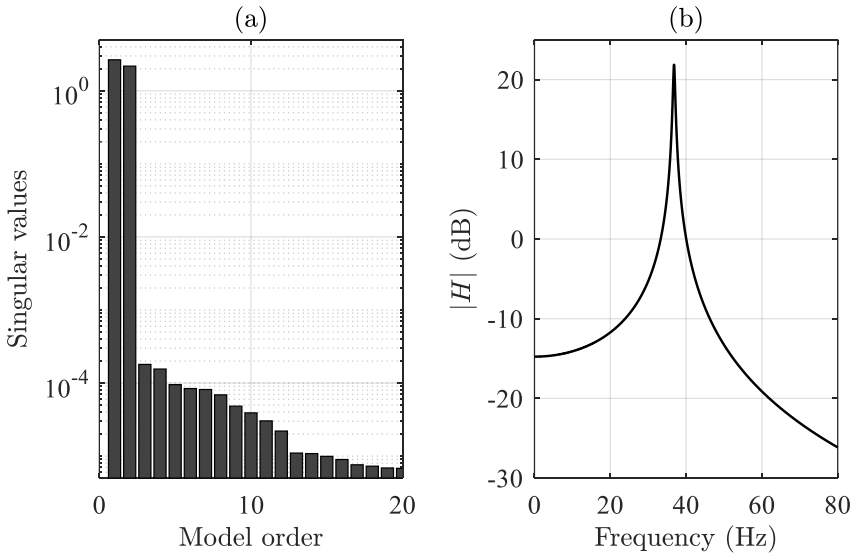

Fig. 3. Electronic Duffing, broadband linear test. Singular values in (a), identified FRF in (b).

3.2. Nonlinear system identification

ACBC method was adopted to obtain the non-parametric frequency response of the system around its primary resonance with an input level of 0.2 V. Fig. 4 illustrates the maximum amplitudes of each harmonic contribution $Y^{(h)}$ up to the 15$^{\text{th}}$ order across the entire NFR, plotted in logarithmic scale. The system response is mainly governed by the fundamental harmonic, followed by the third (approximately

1.5% of the fundamental) and the second harmonic (approximately 0.5% of the fundamental). Minor contributions arise from higher harmonics and eventually approach the noise level, indicated with a dashed red line and estimated from a free-decay test. Given these considerations, nine harmonics ($H = 9$) are retained in the identification process. The complete output vector $\boldsymbol{Y}$ containing all the considered harmonic contributions, along with the input vector $\boldsymbol{F}$, form the input-output dataset $\mathcal{D}\{\boldsymbol{F}(\omega, H), \boldsymbol{Y}(\omega, H)\}$ used for the identification.

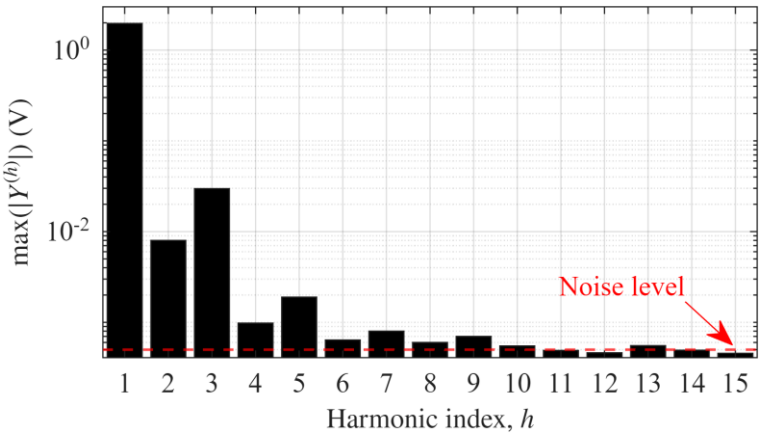

Fig. 4. Electronic Duffing, maximum amplitude of the single harmonic contributions in logarithmic scales.

Quadratic and cubic functions of the output voltage are used as nonlinear basis functions, thus yielding $\boldsymbol{g}_{\mathrm{NL}} = [-y^2, \ -y^3]^{\mathrm{T}}$. The state-space matrices of the nonlinear model have therefore the following sizes: $\boldsymbol{A} \in \mathbb{R}^{2\times2}, \boldsymbol{B}^{\mathrm{e}} \in \mathbb{R}^{2\times3}, \boldsymbol{C} \in \mathbb{R}^{1\times2}, \boldsymbol{D}^{\mathrm{e}} \in \mathbb{R}^{1\times3}$. This gives a total number of parameters to be optimized equal to 15. It is worth noting that the system is not designed to exhibit quadratic nonlinearity in principle, but the latter is expected to be present due to inevitable offsets in the electronics. Nonlinear system identification is carried out following the flowchart of Fig. 1, and the results are displayed in Fig. 5, where the first harmonic of the system response is denoted as $Y^{(1)}$. The norm of the residuals drops from 230 to 0.1 in 2 iterations (Fig. 5a), obtaining the nonlinear frequency response curve of Fig. 5b (circled red line), which is compared to the measured one (black line). The modal parameters of the ULS can be estimated by eigenvalue decomposition of the identified state matrix $\boldsymbol{A}$ of the optimized model. The results are listed in Table 1 and compared to the initial linear model (from low-level broadband test).

Table 1. Electronic Duffing, modal parameters of the ULS.

	Natural frequency (Hz)	Damping ratio (%)
Initial linear model	36.82	0.74
Final nonlinear model (ULS)	36.89	0.75

The coefficients of the nonlinear terms k_2 and k_3 can be estimated from the optimized state-space model as in NSI method (Anastasio and Marchesiello, 2023; Marchesiello and Garibaldi, 2008). This

gives the following values: $k_2 = 0.003\,V^{-1}, k_3 = 1.06\,V^{-2}$. The algorithm took approximately 5 seconds to run (Intel Core i7 @ 2.80 GHz, 16 GB of RAM).

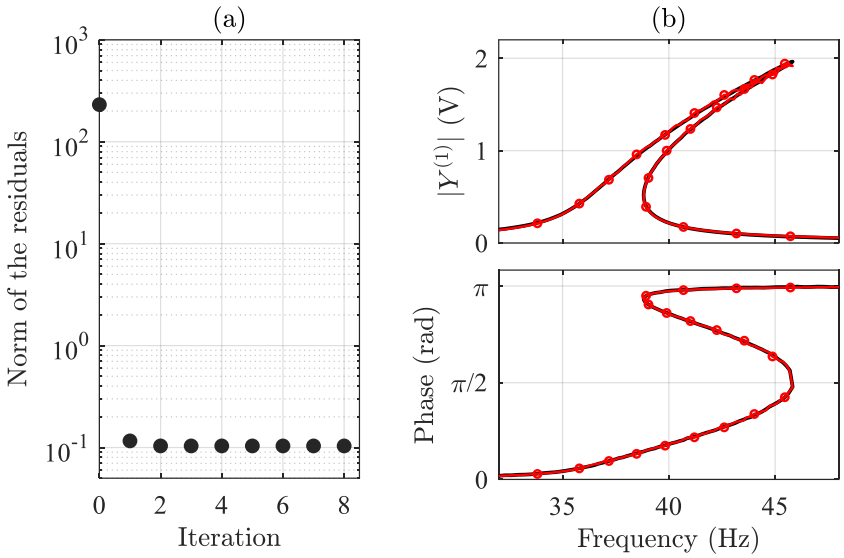

Fig. 5. Electronic Duffing, nonlinear system identification, 0.2 V. Norm of the residuals in (a), amplitude and phase of the response (first harmonic) in (b). Black line: ACBC. Circled line: NFR-ID.

3.3. Validation

The identified model is validated considering two measurements: a high-level (nonlinear) broadband test, and an experimental continuation test (ACBC) with an input level of 0.1 V. Model extrapolation is avoided in both cases, as outlined in (Anastasio et al., 2023). The first test returns a normalized RMS fit value of 94%, which is considered a satisfactory result. The output signal of the validation set $y_{\mathrm{v}}(t)$ is displayed in Fig. 6, along with the model residual $(y_{\mathrm{v,m}}(t) - y_{\mathrm{v}}(t))$, with $y_{\mathrm{v,m}}$ output of the simulation. Fig. 7 presents the result for the second validation set, showing the amplitude and phase of the first harmonic response. The experimental data (black line) and model predictions (red circles) are nearly indistinguishable, indicating a strong agreement. Additionally, the model output reveals an unstable path (dotted red line) caused by a fold bifurcation, as expected in this case.

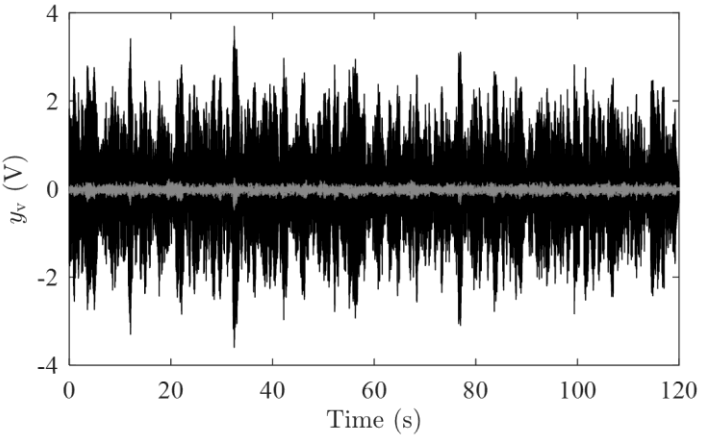

Fig. 6. Electronic Duffing, validation with a random test, 1 V RMS. Black line: measured output; gray line: NFR-ID, model residual.

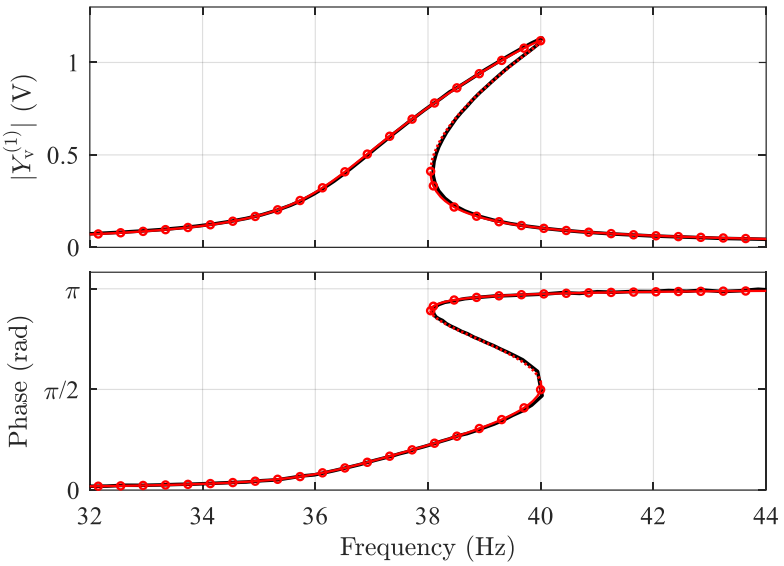

Fig. 7. Electronic Duffing, validation with experimental continuation, 0.1 V. Amplitude and phase of the response (first harmonic). Black line: ACBC. Circled red line: NFR-ID, stable paths. Dotted red line: NFR-ID, unstable paths.

3.4. Robustness to noise

The electronic Duffing system provides a repeatable benchmark, making it a valid candidate for a controlled study on noise. The robustness of the NFR-ID method to noise is assessed by artificially corrupting the experimental output with additive Gaussian noise. Noise is added to the complex-valued output data $\boldsymbol{Y}(\omega, H)$, with a standard deviation defined as a percentage p of the local signal standard deviation. The noisy dataset is denoted $\boldsymbol{Y}_{\mathrm{n}}$.

Ten noise levels were investigated, with p ranging from 1% to 10%. For each level, 100 Monte Carlo simulations were performed to ensure statistical relevance. The results are summarized in Fig. 8. Subplot (a) compares the nonlinear frequency response with 10% added noise to the original curve, showing the noisy data (red dashed-dotted line) visibly scattered around the original NFR (black line). Subplot (b) summarizes the results of the Monte Carlo simulations. The black line represents the norm of the added noise $\left|\left|Y - Y_{\mathrm{n}}\right|\right|$, while the red line shows the model residual $\left|\left|Y_{\mathrm{m}} - Y_{\mathrm{n}}\right|\right|$. The model error starts at 0.1 in the noise-free case and increases with noise level until it follows the trend of the added noise, confirming the consistency of the method. For very high noise levels ($p > 9\%$), the error grows more sharply, reflecting the difficulty of model identification when noise begins to dominate the dynamic response. The increasing size of the shaded regions for higher noise levels reflects the increased variability of the identified models, which is a typical feature of system identification in strongly noisy conditions.

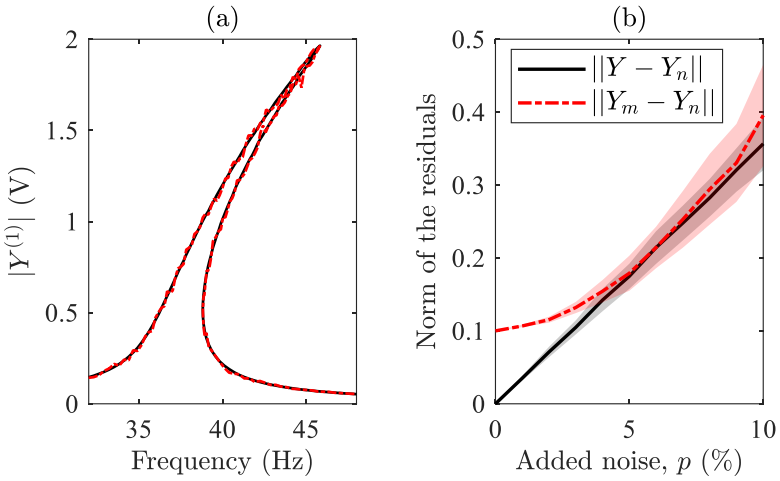

Fig. 8. Electronic Duffing, robustness to noise. (a) Response amplitude without added noise (black line) and with 10% added noise (dashed-dotted red line). (b) Results of the Monte Carlo simulations. The black line represents the norm of the added noise (data residual), and the dashed-dotted red line represents the norm of the model residual. The shaded regions represent the standard deviation across all simulations.

4. Experimental application: clamped-free nonlinear thin plate

A thin, rectangular steel plate measuring 500 mm × 300 mm × 0.5 mm, clamped along its shortest edges, was selected for the next experimental setup as a benchmark for thin-walled structural elements commonly found in civil and mechanical systems. The plate was excited using an electrodynamic shaker (TIRA TV 51075) operating in current mode, while its response was recorded using an impedance head (DYTRAN 5860B), seven accelerometers (DYTRAN 3035B6), and a laser vibrometer (Polytec NLV-2500-5). Fig. 9 shows a picture of the clamped-free plate. It is worth noting that shaker-structure interaction has a non-negligible influence in this setup. When a harmonic drive signal is applied to the amplifier of the shaker, the amplitude of the fundamental forcing harmonic varies with both frequency and amplitude, and harmonics appear in the force signal. To overcome these issues, this study considered the signal supplied to the amplifier, v_{in} (proportional to the current in the shaker), as the system input instead of the force measured by the impedance head. The reader is referred to (Raze et al., 2025) for more insights about these issues.

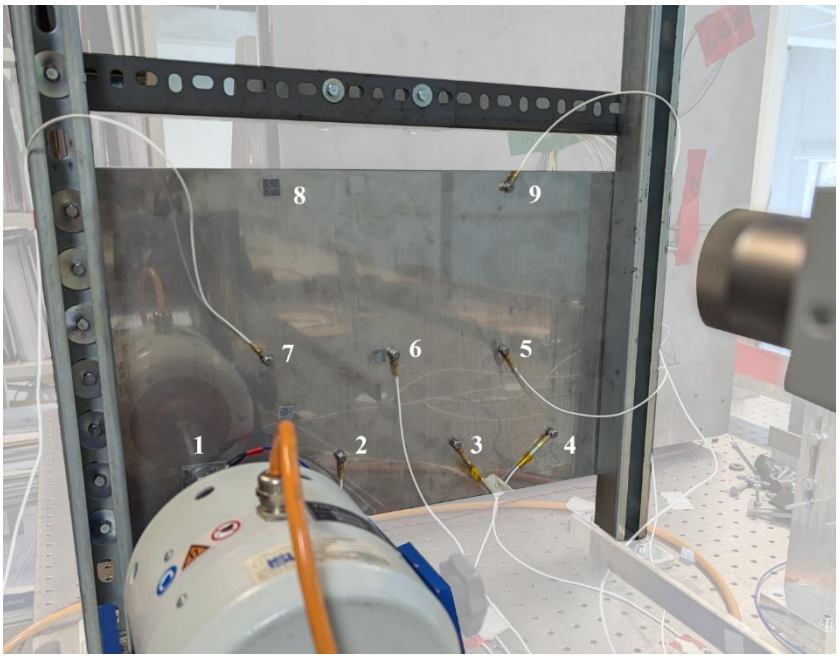

Fig. 9. Clamped-free nonlinear thin plate. The numbers represent the sequence of output measurement channels.

4.1. Assessment of the initial model

The system was first excited with a low-amplitude random signal within the frequency range of [5 100] Hz. Data was sampled at 1600 Hz over a duration of 240 seconds. Linear subspace identification was then applied to estimate the initial linearized state-space model. With a model order of 14, the identified modal parameters are provided in Table 2, while the FRF corresponding to sensor 1 is presented in Fig. 10. Similar results were obtained for the other sensors.

Table 2. Modal parameters of the plate (broadband test).

Mode	Frequency (Hz)	Damping ratio (%)
1	15.43	0.10
2	22.70	1.09
3	38.29	1.34
4	44.14	0.97
5	52.52	1.22
6	66.30	0.60
7	75.19	1.48

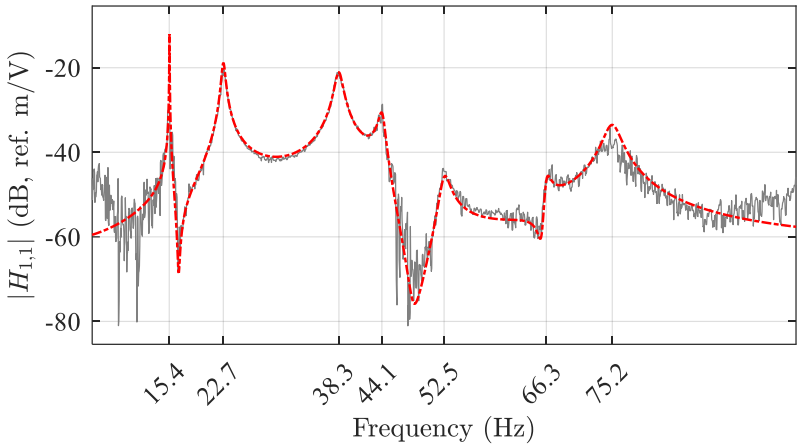

Fig. 10. Plate, driving-point FRF. Gray line: experimental. Dashed-dotted red line: identified.

4.2. Nonlinear system identification

The ACBC method was adopted to obtain the non-parametric frequency responses of the system around its first two resonances considering two input levels: 0.04 V and 0.06 V. The number of harmonics included in the identification process, $H = 9$, was determined from the inspection of the harmonic contributions of the response data. The reader is referred to Section 4.3 for a visualization of the main harmonic components for the 0.04 V level. Fig. 11 shows the amplitude of the 3rd sensor, denoted as $|Y_3|$.

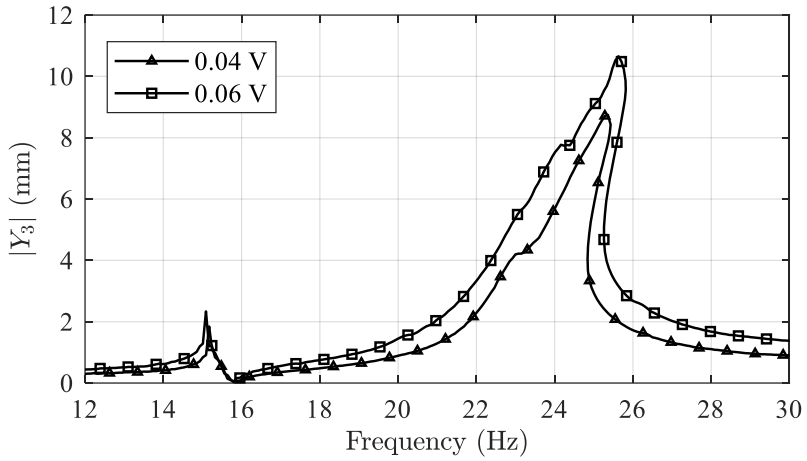

Fig. 11. Plate, experimental continuation for two input levels, sensor 3.

The nonlinear behavior of the system arises from large-amplitude vibrations, leading to a distributed nonlinear strain-displacement relationship. Due to the distributed nature of the nonlinearity, the nonlinear state-space model is identified in a reduced-order domain, using the experimental linear normal modes (LNMs) ϕ as projection basis. This approach is commonly used for this kind of nonlinearity, and reader can refer to (Anastasio et al., 2019; Claeys et al., 2014; Touzé et al., 2004; Touzé and Amabili, 2006) for more insights. The physical displacements $y(x,t)$ are thus written as:

$$y(x,t) \cong \sum_{r=1}^{M} \phi_r(x)\gamma_r(t), \tag{14}$$

with $\gamma_r(t)$ the r^{th} modal coordinate. The term *modal* here is adopted in relation to the reduced-order domain, although LNMs do not decouple the equation of motions in a nonlinear setting.

When applied to experimental continuation, the NFR in modal coordinates is obtained by applying the inverse transformation of eq. (14). Eq. (7) can be written in the reduced-order domain as follows:

$$\begin{cases} (\boldsymbol{\nabla} \otimes \boldsymbol{I}_{2M})\boldsymbol{X} = (\boldsymbol{I}_{\tilde{H}} \otimes \boldsymbol{A})\boldsymbol{X} + (\boldsymbol{I}_{\tilde{H}} \otimes \boldsymbol{B}^{\mathrm{e}})\boldsymbol{Q}^{\mathrm{e}} \\ \boldsymbol{I}_{M\tilde{H}}\boldsymbol{\Gamma} = (\boldsymbol{I}_{\tilde{H}} \otimes \boldsymbol{C})\boldsymbol{X} + (\boldsymbol{I}_{\tilde{H}} \otimes \boldsymbol{D}^{\mathrm{e}})\boldsymbol{Q}^{\mathrm{e}} \end{cases}, \tag{15}$$

where $M = 2$ is the number of considered modes, $\boldsymbol{\Gamma}$ is the output vector in modal coordinates and $\boldsymbol{Q}^{\mathrm{e}} = \left[\boldsymbol{Q}^{\mathrm{T}}, \quad \boldsymbol{G}_{\mathrm{nl}}^{\mathrm{T}}\right]^{\mathrm{T}}$ is the extended input vector. The generalized modal forces $\boldsymbol{Q}$ are obtained from v_{in} and the LNMs.

The vector $\boldsymbol{G}_{\mathrm{nl}}$ is computed using AFT technique also in this case, considering a polynomial expansion of the modal coordinates $\gamma_{1,2}$ up to the selected orders a, b. This yields:

$$\boldsymbol{g}_{\mathrm{nl}}(t) = \left[-\gamma_1^2, \quad \dots, \quad -\gamma_1^a, \quad -\gamma_2^2, \quad \dots, \quad -\gamma_2^b\right]^{\mathrm{T}}. \tag{16}$$

The maximum grades a and b for γ_1 and γ_2 are selected based on the norm of the residuals obtained with the optimization procedure, and they are varied in the range [3:8]. The combination of grades giving the best results is $a = 5, b = 7$, with a residual norm of 3.2×10^{-5}. By comparison, the initial linear model returns a residual norm of 0.01, roughly three orders of magnitude larger than the optimized nonlinear one. In this case, the optimization process includes 90 parameters, with a computational time of approximately 37 seconds on an Intel Core i7 (2.80 GHz, 16 GB of RAM). Further details on model correlations are provided in Appendix A.

The experimental (black lines) and identified (circled red lines) NFRs of the two modal coordinates are represented in Fig. 12. The two curves exhibit strong agreement within the resonance regions. However, some discrepancies are noticeable in $\left|\Gamma_1^{(1)}\right|$ near the second resonance region. The modelled NFRs with $a = b = 3$ is also represented as a comparison (squared blue line).

Given the complexity of the nonlinear model, an additional analysis was conducted to determine the robustness of the algorithm to the initial (linear) guess. The whole identification process was repeated multiple times, each using a distinct linear initial model identified from a portion of the original 240-second low-amplitude data. The size of these data portions ranged from 10% to 50% of the total length. The analysis confirmed the robustness of the method, returning an average residual norm of 4×10^{-5}, with a standard deviation of 1×10^{-5}.

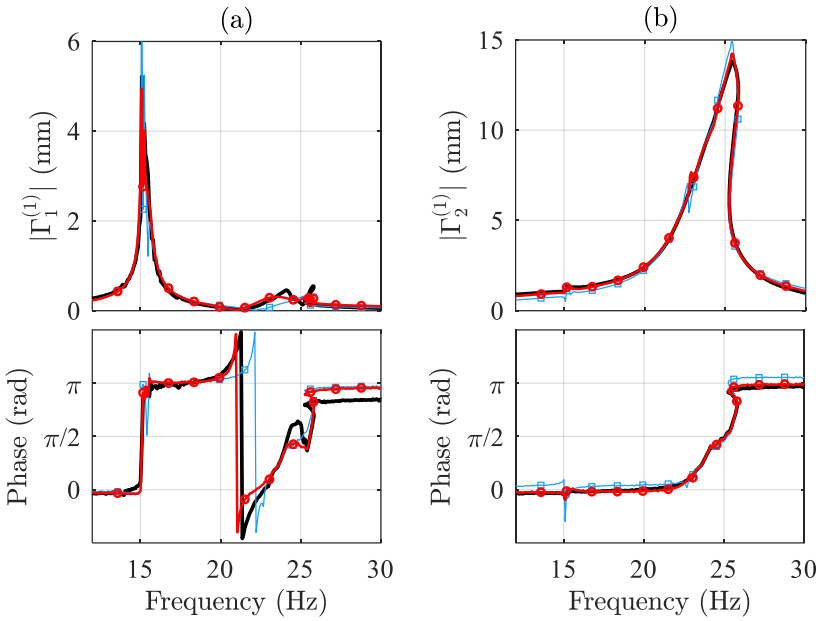

Fig. 12. Plate, modal NFR (first harmonic), 0.06 V. First modal coordinate in (a), second modal coordinate in (b). Black line: ACBC. Circled red line: NFR-ID, final model. Squared blue line: NFR-ID, *a=b=3*.

4.3. Validation

The identified model is validated considering two different measurements: experimental continuation (ACBC) with input level of 0.04 V and frequency sweep with input level of 0.05 V. Fig. 13 illustrates the validation results with respect to ACBC, showing the amplitude and phase of the modal coordinates for the first harmonic. Similar to Fig. 12, the two curves exhibit very good overall agreement. Notably, the model predicts slightly more pronounced softening behavior at the first resonance (around 15 Hz), compared to experimental observations. Some discrepancies are also present in $\left|\Gamma_{v,1}^{(1)}\right|$ near the region of the second resonance. The model output also reveals unstable paths (dotted red lines) associated with fold bifurcations.

To further investigate the behavior of higher harmonics, Fig. 14 displays the maximum amplitude of each harmonic contribution in the modal domain for both experimental (black bars) and predicted (red bars) cases. In both instances, the first harmonic dominates the response, although contributions up to the 7th harmonic can be observed. The predicted harmonic contributions closely resemble the experimental results, with percentage differences of 1.17% and 0.2% for the first and second modal coordinates, respectively.

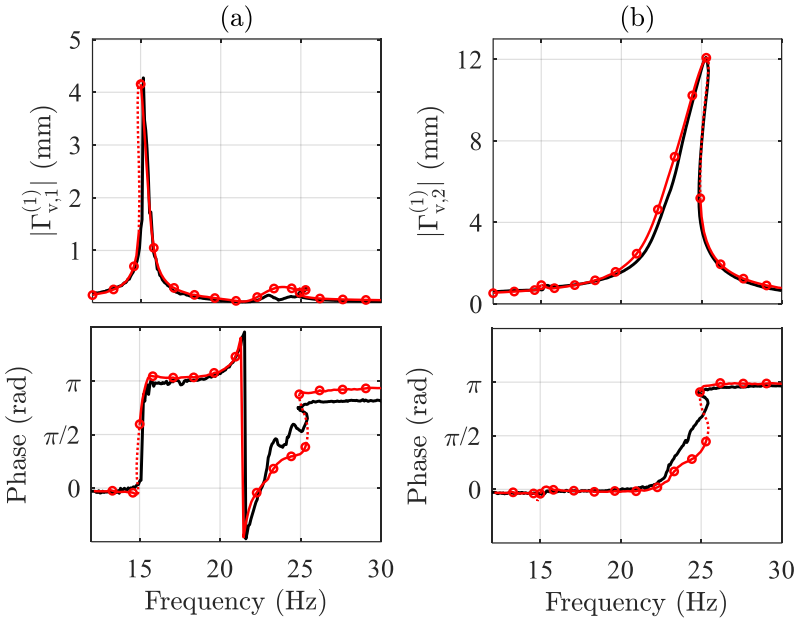

Fig. 13. Plate, validation with experimental continuation, 0.04 V. First modal coordinate in (a), second modal coordinate in (b). Black line: ACBC. Circled red line: NFR-ID, stable paths. Dotted red line: NFR-ID, unstable paths.

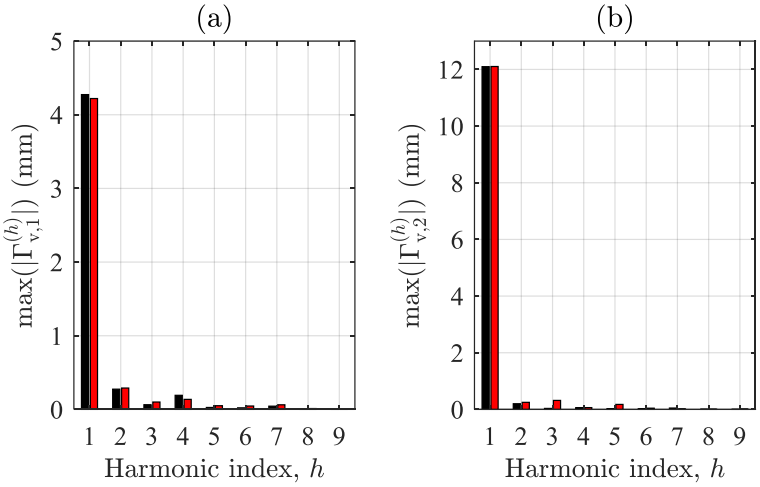

Fig. 14. Plate, validation with experimental continuation, 0.04 V. Maximum amplitude of the single harmonic contributions. ACBC in black, NFR-ID in red. First modal coordinate in (a), second modal coordinate in (b).

The simulated frequency responses are converted to the physical domain by applying the inverse transformation of eq. (14). The RMS fit values of the predicted NFR amplitudes against measured ones can be determined by resampling the frequency axis of the numerical continuation to align with the experimental one. This results in an average fit of 91% across all sensors, as shown in Fig. 15 (dashed red line), which is considered a satisfactory result.

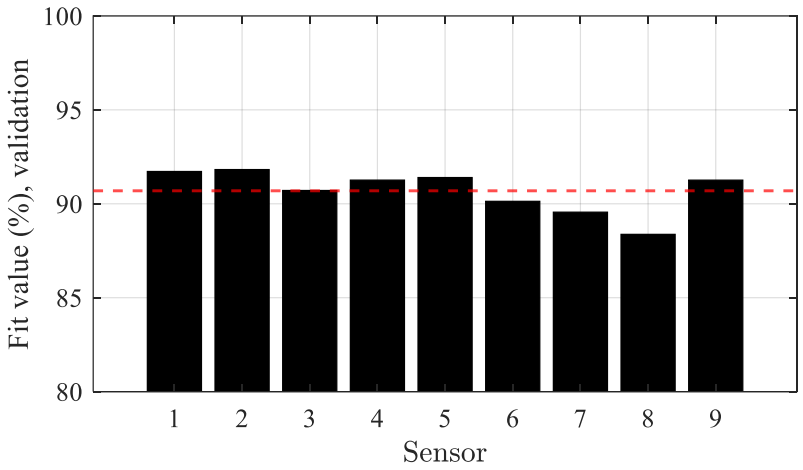

Fig. 15. Plate, validation with experimental continuation, 0.04 V. Black bars: RMS fit values across all the sensors. Dashed red line: average value.

A final comparison for this validation set is conducted by analyzing the measured and predicted operating deflection shapes (ODSs) at the two resonance peaks. These are evaluated against the corresponding LNMs in Table 3 and Table 4 by computing the corresponding MAC matrix. Experimental and identified values show a perfect match (MAC value nearly equal to 1). It should be noted that MAC values approaching unity only indicate that the identified model accurately captures the shape of the vibration pattern at resonances, not necessarily the amplitude, which can be observed in Fig. 13. While the first ODS shows a slight deviation from the first LNM, the second ODS is nearly identical to its corresponding LNM.

Table 3. MAC of the first ODS.

	ϕ_1	$\mathrm{ODS}_1 - \mathrm{exp.}$	$\mathrm{ODS}_1 - \mathrm{id.}$
ϕ_1	1.0000	0.9743	0.9761
$\mathrm{ODS}_1 - \mathrm{exp.}$	0.9743	1.0000	0.9925
$\mathrm{ODS}_1 - \mathrm{id.}$	0.9761	0.9925	1.0000

Table 4. MAC of the second ODS.

	ϕ_2	$\mathrm{ODS}_2 - \mathrm{exp.}$	$\mathrm{ODS}_2 - \mathrm{id.}$
ϕ_2	1.0000	0.9993	0.9995
$\mathrm{ODS}_2 - \mathrm{exp.}$	0.9993	1.0000	0.9999
$\mathrm{ODS}_2 - \mathrm{id.}$	0.9995	0.9999	1.0000

Fig. 16 illustrates the results for the second validation set. The system was driven through linear frequency sweeps, both upward and downward, around the second mode at a rate of 0.05 Hz/s. The measured input signal amplitude was then fed to the identified state-space model to obtain the corresponding NFR curves. The amplitude of the oscillations predicted by the NFR-ID approach closely match the measured ones, confirming the effectiveness of the method. An unstable path is visible also in this case (dotted line), and coherent with experimental jump frequencies.

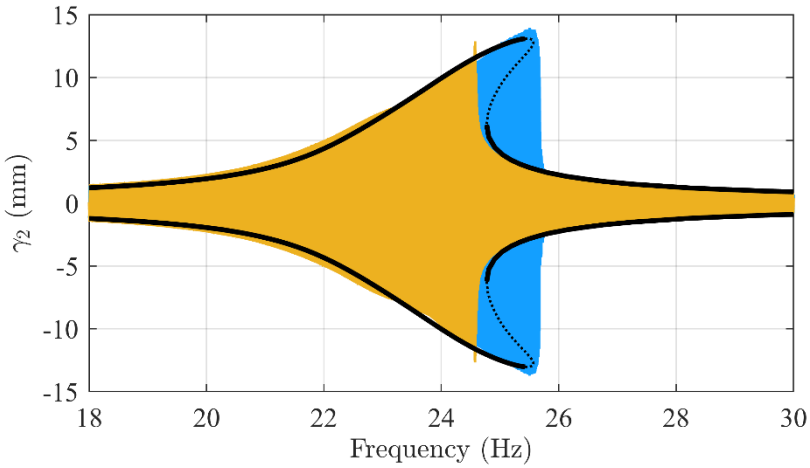

Fig. 16. Plate, validation with frequency sweep tests, 0.05 V. Blue line: sweep-up. Yellow line: sweep-down. Continuous black line: NFR-ID, stable path. Dotted black line: NFR-ID, unstable path.

5. Conclusions

This study introduced NFR-ID, a data-based modeling approach that estimates an interpretable and nonlinear state-space model from frequency response data. A central contribution of the framework is its ability to exploit experimental continuation data, including unstable branches, by minimizing the residual between measured and predicted outputs across multiple harmonics. This enables accurate characterization of nonlinear dynamics using limited datasets, while keeping computational costs low and ensuring robustness to noise and initialization. The method was validated on two experimental setups: an electronic Duffing oscillator and a clamped-free thin plate. The former serves as a classic SDOF benchmark for nonlinear system identification algorithms, while the latter exhibits strong and complex nonlinear behavior at its first two resonances, arising from large amplitude vibrations.

Overall, the ability of NFR-ID to accurately reconstruct both simple and complex nonlinear behaviors from frequency-domain data, including unstable responses, highlights its potential as an efficient and general tool for data-based modeling in structural dynamics and related engineering applications. The chosen model structure enables direct interpretability of the results, offering insights into the system characteristics. Additionally, the proposed methodology is compatible with frequency swept-sine tests, that are routinely performed for nonlinear structures. Nevertheless, the method relies on prior characterization to select an appropriate set of nonlinear basis functions, which might be challenging. Looking ahead, further developments could include adaptive selection of nonlinear basis functions, enhanced noise-handling strategies, and alternative optimization schemes to strengthen convergence robustness.

Appendix A: Parameter correlation matrix

The parameter correlation matrix $\mathbf{Corr}_\theta$ provides insights into the identifiability and interdependence of the estimated parameter vector $\boldsymbol{\theta}$. It is obtained by normalizing the covariance matrix $\mathbf{Cov}_\theta$ with the standard deviations of the parameters:

$$\mathrm{Corr}_\theta(i,j) = \frac{\mathrm{Cov}_\theta(i,j)}{\mathrm{std}(\theta_i)\cdot\mathrm{std}(\theta_j)}.$$

Values of $\mathbf{Corr}_\theta$ close to ± 1 indicate strong correlation, whereas values near zero suggest independence. High correlations highlight directions in the parameter space that are not independently identifiable, often due to redundancy in the model structure.

The correlation matrix associated with the 90 parameters of Section 4 is displayed in Fig. A.1. The correlations exhibit a structured pattern corresponding to the internal architecture of the reduced-order nonlinear state-space model. The strong red diagonal confirms that each parameter is perfectly correlated with itself, as expected. Moderate to high off-diagonal correlations appear mainly within the $\boldsymbol{B}^{\mathrm{e}}$ and $\boldsymbol{D}^{\mathrm{e}}$ blocks, consistent with the use of non-orthogonal polynomial basis functions to model the nonlinearities. As for the reduced-order state matrix $\boldsymbol{A}$, moderate correlations arise as a consequence of the optimization process, which produces non-zeros off-diagonal blocks coupling the parameters that govern the underlying linear dynamics. Cross-block correlations remain generally weak.

Although certain parameters exhibit strong correlations, the overall identifiability of the model is considered satisfactory. The combination of a low residual norm and consistent validation results confirm the robustness of the identified model and its reliability in predicting the dynamic behavior of the system.

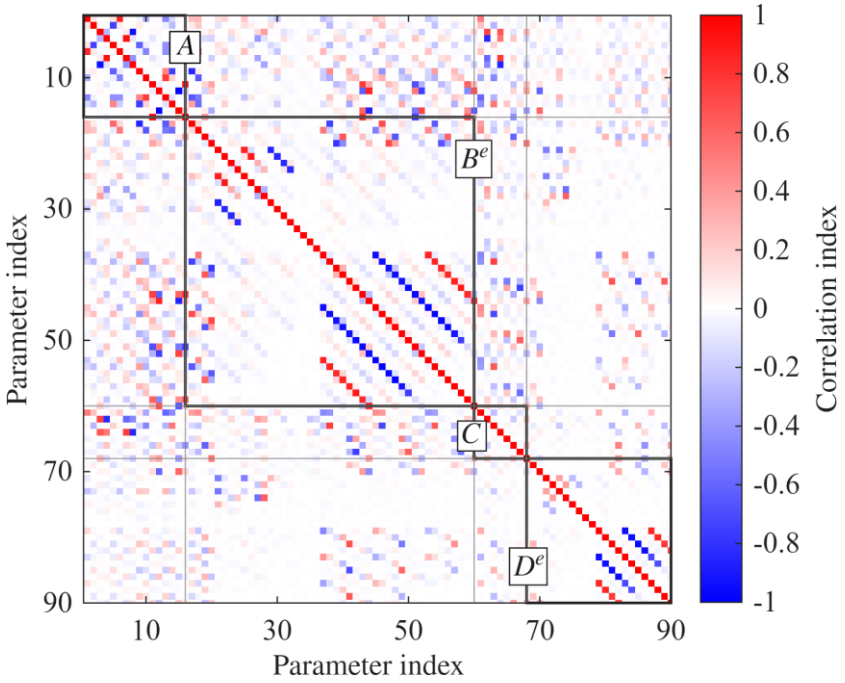

Fig. A.1. Parameter correlation matrix for the identified model of Section 4.

References

Abeloos G, Renson L, Collette C, et al. (2021) Stepped and swept control-based continuation using adaptive filtering. *Nonlinear Dynamics* 104(4): 3793–3808.

Anastasio D and Marchesiello S (2023) Nonlinear frequency response curves estimation and stability analysis of randomly excited systems in the subspace framework. *Nonlinear Dynamics* 111(9): 8115–8133.

Anastasio D, Marchesiello S, Kerschen G, et al. (2019) Experimental identification of distributed nonlinearities in the modal domain. *Journal of Sound and Vibration* 458. Academic Press: 426–444.

Anastasio D, Marchesiello S, Gatti G, et al. (2023) An investigation into model extrapolation and stability in the system identification of a nonlinear structure. *Nonlinear Dynamics* 111(19): 17653–17665.

Arslan Ö, Aykan M and Nevzat Özgüven H (2011) Parametric identification of structural nonlinearities from measured frequency response data. *Mechanical Systems and Signal Processing* 25(4): 1112–1125.

Barton DA, Mann BP and Burrow SG (2012) Control-based continuation for investigating nonlinear experiments. *Journal of Vibration and Control* 18(4). SAGE Publications: 509–520.

Barton DAW and Sieber J (2013) Systematic experimental exploration of bifurcations with noninvasive control. *Physical Review E* 87(5): 052916.

Beregi S, Barton DAW, Rezgui D, et al. (2021) Robustness of nonlinear parameter identification in the presence of process noise using control-based continuation. *Nonlinear Dynamics* 104(2): 885–900.

Cameron TM and Griffin JH (1989) An Alternating Frequency/Time Domain Method for Calculating the Steady-State Response of Nonlinear Dynamic Systems. *Journal of Applied Mechanics* 56(1). 1: 149–154.

Canbaloğlu G and Özgüven HN (2016) Model updating of nonlinear structures from measured FRFs. *Mechanical Systems and Signal Processing* 80: 282–301.

Carrella A and Ewins DJ (2011) Identifying and quantifying structural nonlinearities in engineering applications from measured frequency response functions. *Mechanical Systems and Signal Processing* 25(3): 1011–1027.

Claeys M, Sinou JJ, Lambelin JP, et al. (2014) Multi-harmonic measurements and numerical simulations of nonlinear vibrations of a beam with non-ideal boundary conditions. *Communications in Nonlinear Science and Numerical Simulation* 19(12). 12. Elsevier: 4196–4212.

Demarie GV, Ceravolo R, Sabia D, et al. (2011) Experimental identification of beams with localized nonlinearities. *Journal of Vibration and Control* 17(11). SAGE Publications: 1721–1732.

Detroux T, Renson L, Masset L, et al. (2015) The harmonic balance method for bifurcation analysis of large-scale nonlinear mechanical systems. *Computer Methods in Applied Mechanics and Engineering* 296. Elsevier: 18–38.

Feldman M, Bucher I and Rotberg J (2009) Experimental Identification of Nonlinearities under Free and Forced Vibration using the Hilbert Transform. *Journal of Vibration and Control* 15(10). SAGE Publications: 1563–1579.

Gatti G, Brennan MJ and Tang B (2019) Some diverse examples of exploiting the beneficial effects of geometric stiffness nonlinearity. *Mechanical Systems and Signal Processing* 125. Academic Press: 4–20.

Jalali H and Bonab BT (2013) Nonlinearity identification using sensitivity of frequency response functions. *Journal of Vibration and Control* 19(5). SAGE Publications: 787–800.

Karaağaçlı T and Özgüven HN (2020) A frequency domain nonparametric identification method for nonlinear structures: Describing surface method. *Mechanical Systems and Signal Processing* 144. Academic Press.

Karaağaçlı T and Özgüven HN (2021) Experimental modal analysis of nonlinear systems by using response-controlled stepped-sine testing. *Mechanical Systems and Signal Processing* 146. Academic Press.

Kerschen G, Worden K, Vakakis AF, et al. (2006) Past, present and future of nonlinear system identification in structural dynamics. *Mechanical Systems and Signal Processing* 20(3): 505–592.

Kerschen G, Vakakis AF, Lee YS, et al. (2008) Toward a Fundamental Understanding of the Hilbert-Huang Transform in Nonlinear Structural Dynamics. *Journal of Vibration and Control* 14(1–2). SAGE Publications: 77–105.

Kutz JN (ed.) (2016) *Dynamic Mode Decomposition: Data-Driven Modeling of Complex Systems*. Other titles in applied mathematics 149. Philadelphia, Pennsylvania: Society for Industrial and Applied Mathematics (SIAM, 3600 Market Street, Floor 6, Philadelphia, PA 19104).

Levenberg K (1944) A method for the solution of certain non-linear problems in least squares. *Quarterly of Applied Mathematics* 2(2): 164–168.

Maio DD (2025) A novel analysis method for calculating nonlinear Frequency Response Functions. *Journal of Structural Dynamics*. Epub ahead of print 2025. DOI: 10.25518/2684-6500.242.

Marchesiello S and Garibaldi L (2008) A time domain approach for identifying nonlinear vibrating structures by subspace methods. *Mechanical Systems and Signal Processing* 22(1). 1: 81–101.

Marquardt DW (1963) An Algorithm for Least-Squares Estimation of Nonlinear Parameters. *Journal of the Society for Industrial and Applied Mathematics* 11(2): 431–441.

Mélot A, Denimal Goy E and Renson L (2024) Nonlinear system identification with control-based continuation of bifurcation curves. In: *ENOC 2024 - 11th European Nonlinear Dynamics Conference*, Delft, Netherlands, July 2024, pp. 1–2. Available at: https://hal.science/hal-04701315.

Nayfeh AH and Mook DT (1995) *Nonlinear Oscillations*. 1st edn Wiley. Available at: https://onlinelibrary.wiley.com/doi/book/10.1002/9783527617586 (accessed 9 October 2024).

Noël JP and Kerschen G (2013) Frequency-domain subspace identification for nonlinear mechanical systems. *Mechanical Systems and Signal Processing* 40(2): 701–717.

Noël JP and Kerschen G (2017) Nonlinear system identification in structural dynamics: 10 more years of progress. *Mechanical Systems and Signal Processing* 83. Academic Press: 2–35.

Noël JP, Kerschen G, Foltête E, et al. (2014) Grey-box identification of a non-linear solar array structure using cubic splines. *International Journal of Non-Linear Mechanics* 67. Elsevier Ltd: 106–119.

Overschee P van and Moor BL de (1996) *Subspace Identification for Linear Systems: Theory — Implementation — Applications*. Springer US. Available at: https://www.springer.com/gp/book/9781461380610 (accessed 25 October 2021).

Paduart J, Lauwers L, Swevers J, et al. (2010) Identification of nonlinear systems using Polynomial Nonlinear State Space models. *Automatica* 46(4): 647–656.

Peter S and Leine RI (2017) Excitation power quantities in phase resonance testing of nonlinear systems with phase-locked-loop excitation. *Mechanical Systems and Signal Processing* 96: 139–158.

Raze G (2024) An electronic Duffing oscillator. Available at: https://github.com/GhislainRaze/Electronic-Duffing.

Raze G, Abeloos G and Kerschen G (2025) Experimental continuation in nonlinear dynamics: recent advances and future challenges. *Nonlinear Dynamics*. Epub ahead of print 2025. DOI: 10.1007/s11071-024-10543-9.

Sieber J and Krauskopf B (2008) Control based bifurcation analysis for experiments. *Nonlinear Dynamics* 51(3): 365–377.

Taghipour J, Khodaparast HH, Friswell MI, et al. (2022) Harmonic-Balance-Based parameter estimation of nonlinear structures in the presence of Multi-Harmonic response and force. *Mechanical Systems and Signal Processing* 162. Academic Press.

Touzé C and Amabili M (2006) Nonlinear normal modes for damped geometrically nonlinear systems: Application to reduced-order modelling of harmonically forced structures. *Journal of Sound and Vibration* 298(4–5). Academic Press: 958–981.

Touzé C, Thomas O and Huberdeau A (2004) Asymptotic non-linear normal modes for large-amplitude vibrations of continuous structures. *Computers and Structures* 82(31–32). 31–32: 2671–2682.

Worden K and Tomlinson GR (2001) *Nonlinearity in Structural Dynamics: Detection, Identification, and Modelling*. Institute of Physics.

Zhu R, Jiang D, Marchesiello S, et al. (2023) Automatic Nonlinear Subspace Identification Using Clustering Judgment Based on Similarity Filtering. *AIAA Journal* 61(6). American Institute of Aeronautics and Astronautics (AIAA): 2666–2674.